Supporting Information

for *Journal of Materials Chemistry B*

Title: Nanoconfined Crystallites Toughen Artificial Silk

Hui Pan, Yaopeng Zhang, Huili Shao, Xuechao Hu, Xiuhong Li, Feng Tian, Jie Wan*

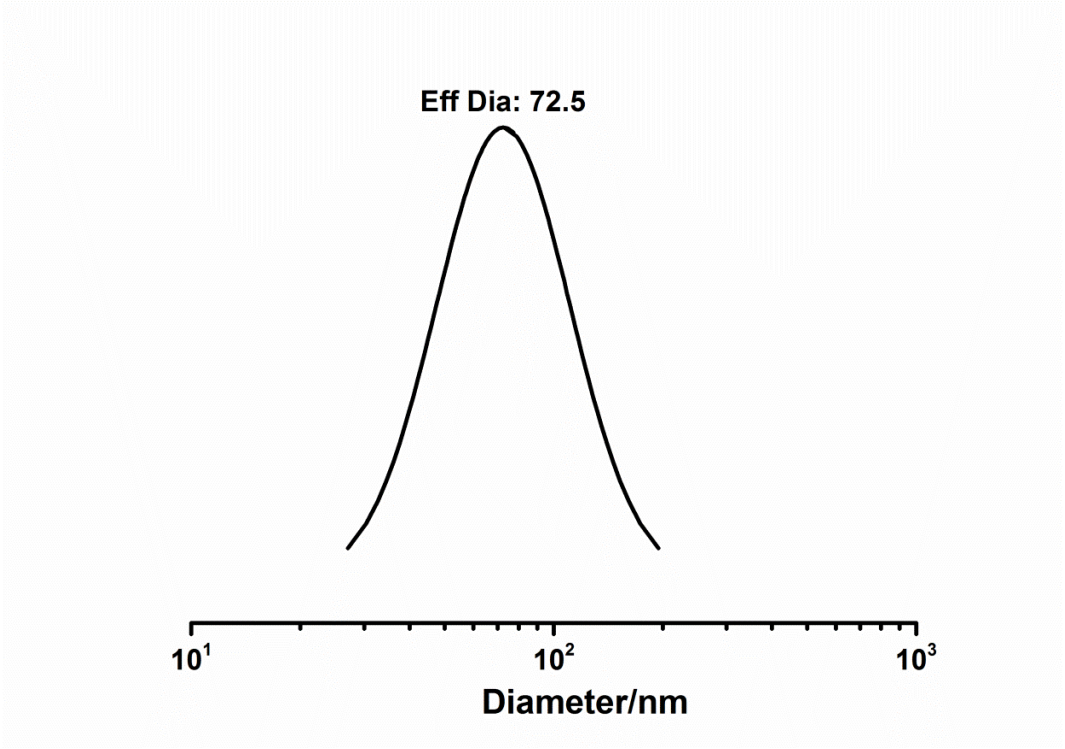

Figure S1. The nano-TiO_2 size distribution tested by dynamic light scattering (DLS). The nano-TiO_2 had a hydrodynamic radius of 72.5 nm obtained by a BI-200SM DLS machine (Brookhaven, USA).

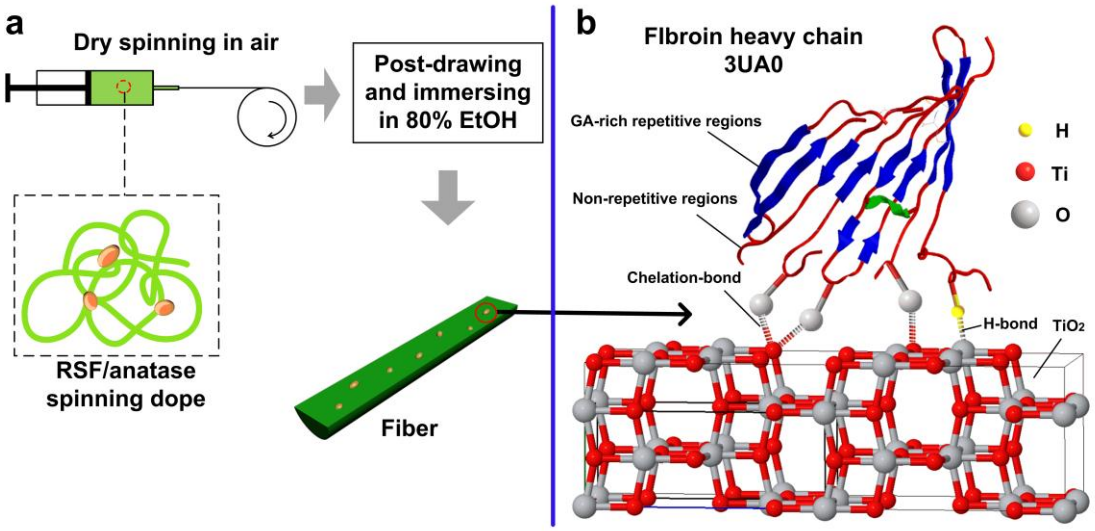

Figure S2. (a) Preparation of nanoanatase-incorporated artificial silk fibers from RSF/anatase spinning dope. (b) Schematic illustration of the interface between silk matrix and nanoanatase. The possible interaction bonds between silk fibroin and TiO_2 are TiO_2/N-terminus (No.1 bond from left), TiO_2/middle segmer (No.2 from left), TiO_2/C-terminus (No.3 bond from left) and H-bond (No.4 from left).

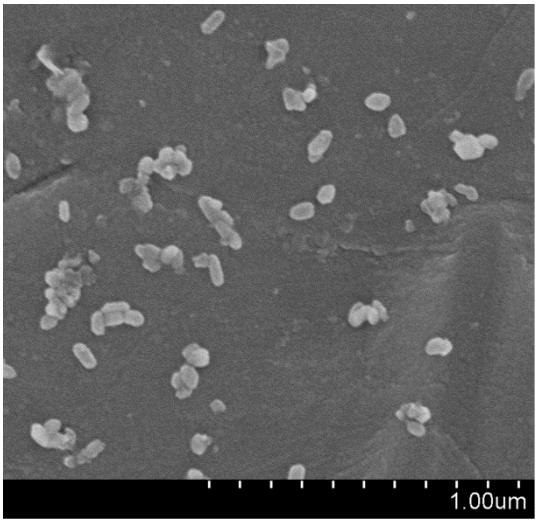

Figure S3. FESEM image of nano-TiO_2. The average dimension of the nano-TiO_2 (Hangzhou Wanjing New Materials Co., Ltd, China) shown was 25×50 nm. This image was obtained by an S-4800 FESEM (HITACHI, Japan).

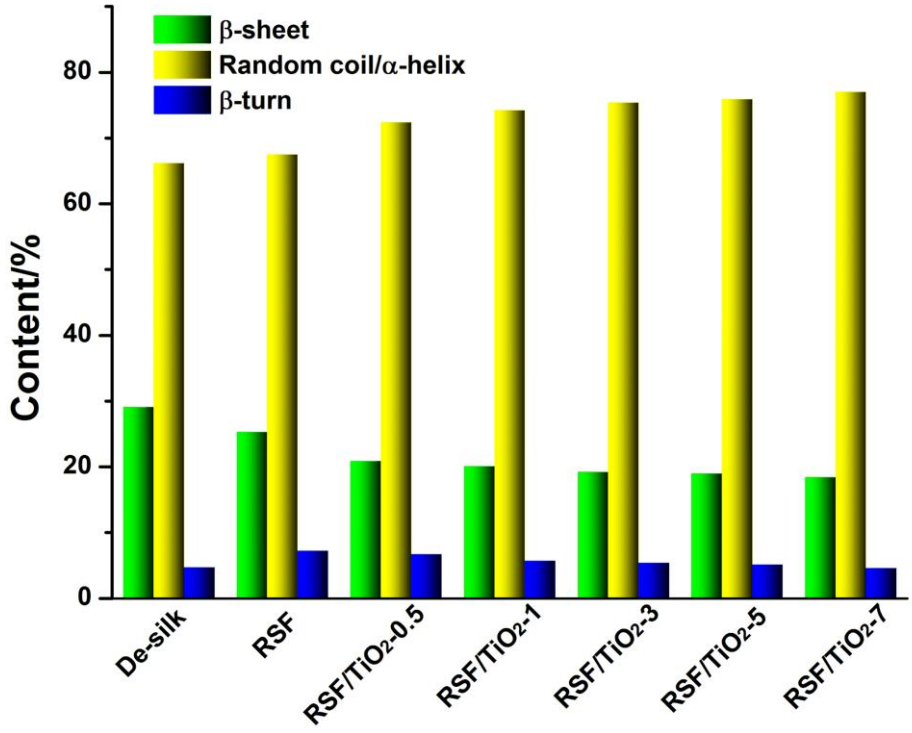

Figure S4. Deconvolution result of FTIR spectra in Amide I band. Comparison of β-sheet and random coil/α-helix conformation contents corresponding to the silks in Figure 3a.

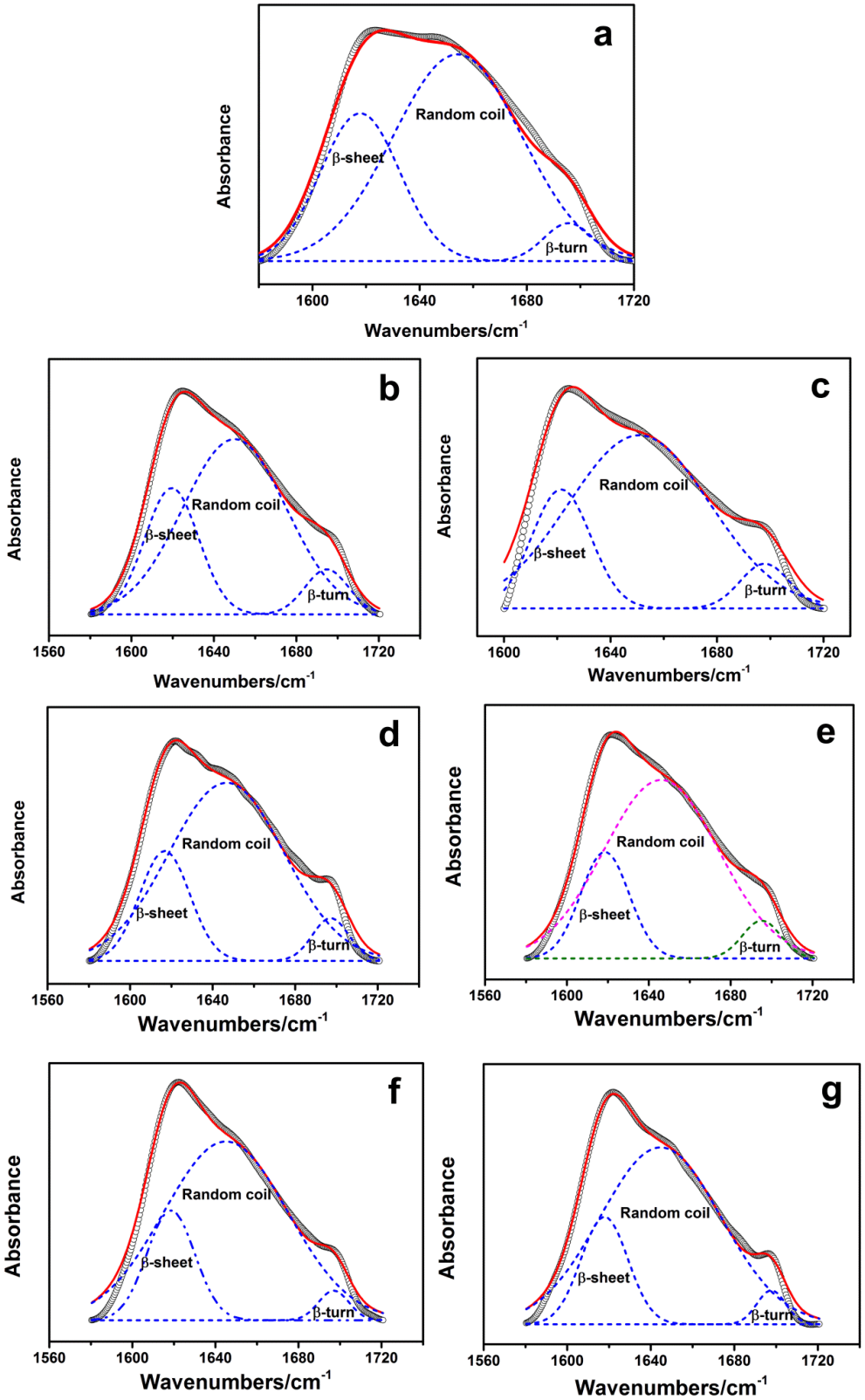

Figure S5. The deconvolution of Fourier-transform infrared (FTIR) spectra in Amide I band. (a) De-silk. (b~g) RSF/TiO_2 hybrid fibers with TiO_2 contents of 0, 5‰, 1‰, 3‰, 5‰ and 7‰, respectively. Circles, original spectrum; dashed curve, deconvoluted peaks; solid curve, simulated spectrum from summed peaks.

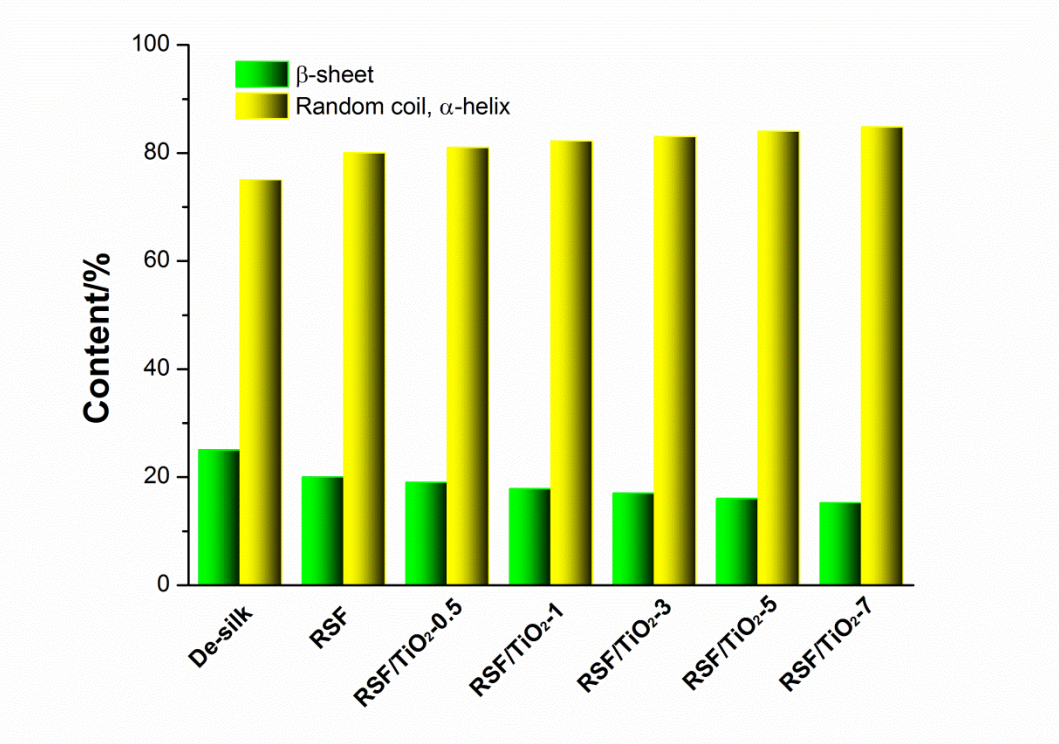

Figure S6. Deconvolution result of FTIR spectra in Amide III band. Comparison of β-sheet and random coil/α-helix conformation contents corresponding to the silks in Figure 3a.

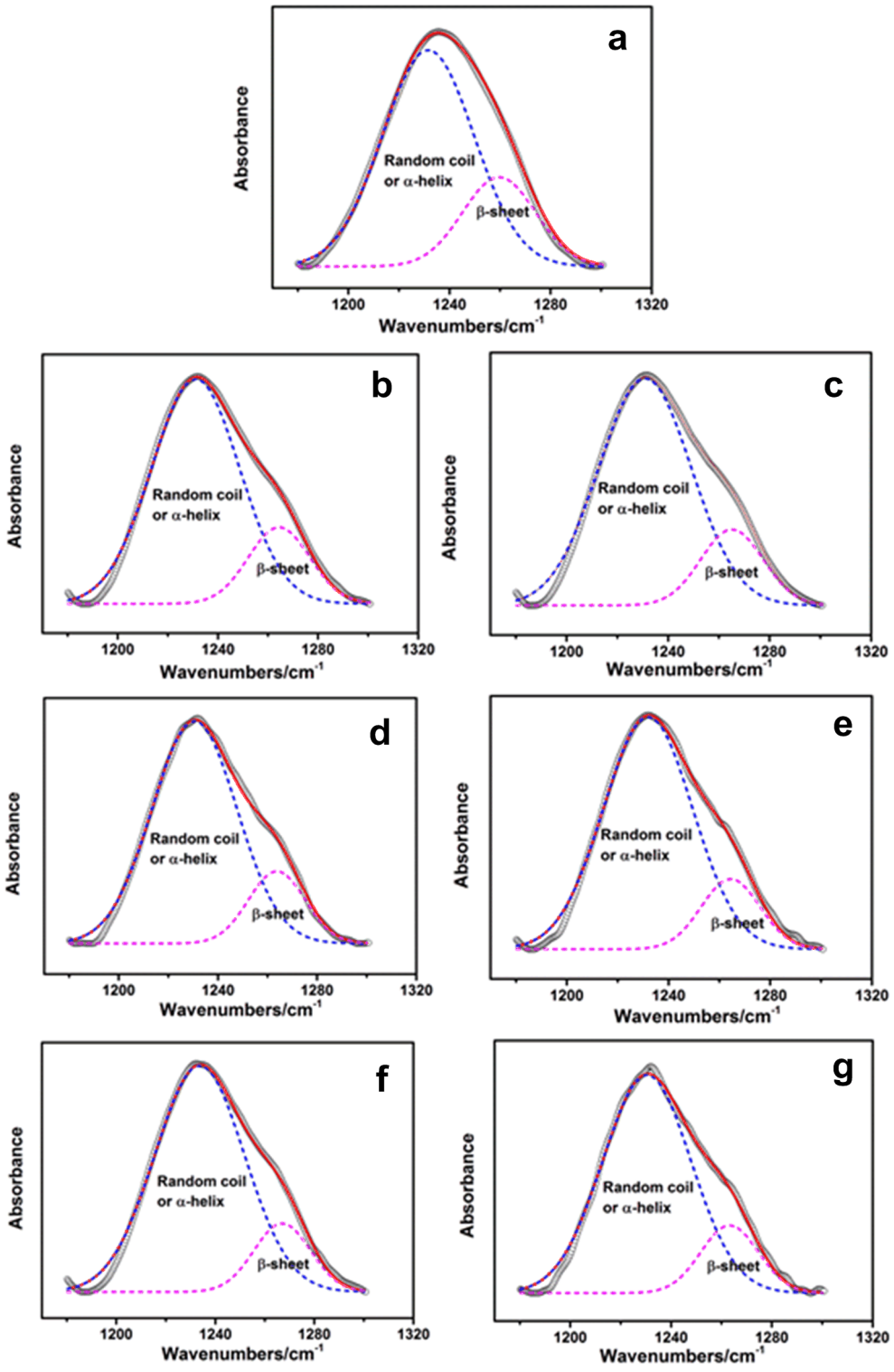

Figure S7. The deconvolution of FTIR spectra in Amide III band. (a) De-silk. (b~g) RSF/TiO_2 hybrid fibers with TiO_2 contents of 0, 5‰, 1‰, 3‰, 5‰ and 7‰, respectively. Circles, original spectrum; dashed curve, deconvoluted peaks; solid curve, simulated spectrum from summed peaks.

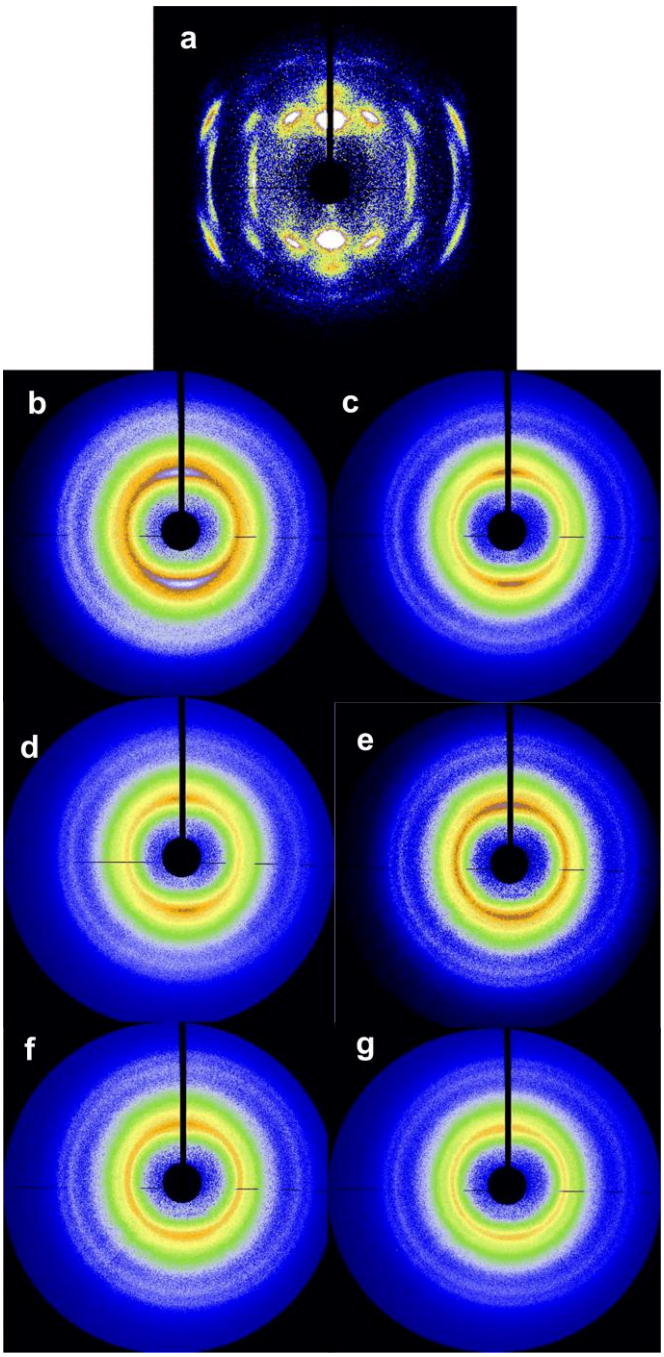

Figure S8. Two-dimensional SR-WAXD patterns of (a) De-silk, (b) RSF fiber and (c) RSF/TiO_2-0.5 fiber, (d) RSF/TiO_2-1 fiber, (e) RSF/TiO_2-3 fiber, (f) RSF/TiO_2-5 fiber, (g) RSF/TiO_2-7 fiber

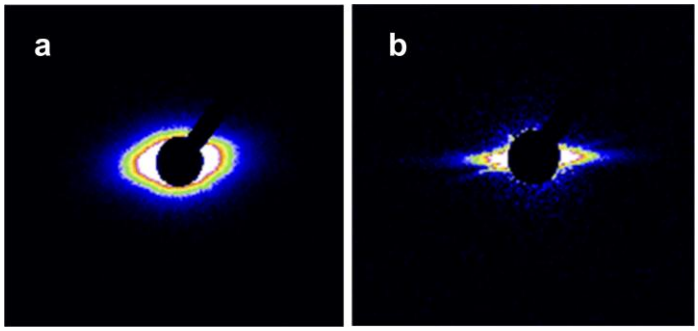

Figure S9. Two-dimensional SR-SAXS patterns of (d) De-silk, and (e) RSF/TiO_2-1 fiber.

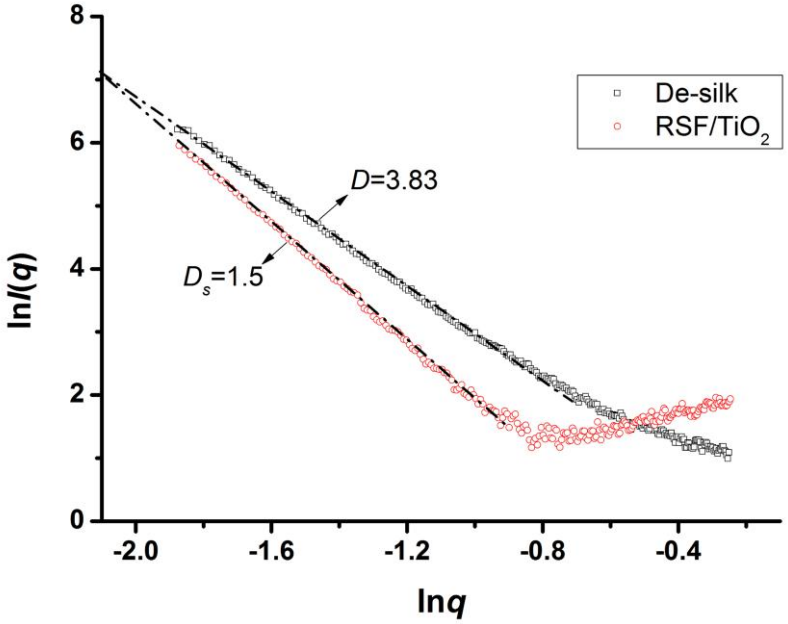

Figure S10. ln$I(q)$-ln$q$ curves of RSF/TiO_2-1 silk and De-silk. D is fractal dimension and D_s is surface fractal dimension for composite.

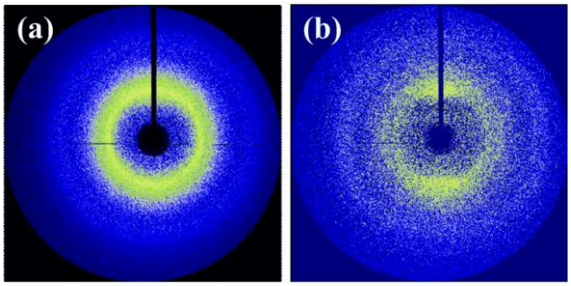

Figure S11. WAXD patterns of RSF/TiO_2 fiber at (a) elastic deformation zone and (b) plastic deformation zone observed in the stress-strain curve of the RSF/TiO_2 fiber. The elastic deformation zone is before the first yield point. The plastic deformation zone is between the first yield point and the second yield point. The loops in (a) indicate the low orientation. The equatorial symmetric pattern in (b) indicates the crystal region orientation. The experiment was taken by synchrotron radiation hard X-ray microfucs diffraction. The single fiber was fixed on a custom-made device which can supply defined load and displacement. Pattern (a) was collected from a single fiber bearing a defined stress which was lower than yield stress. Pattern (b) was collected from the single fiber in defined strain which was larger than yield strain.

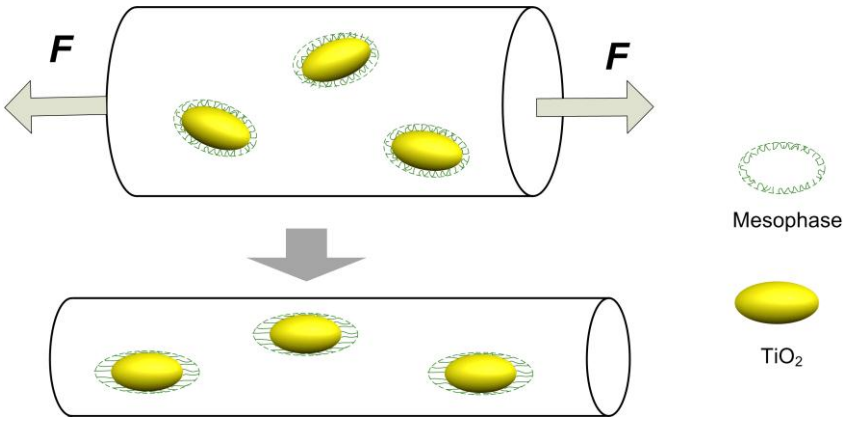

Figure S12. Diagrammatic drawing of the mesophase orientation after the second yield point observed in stress-strain curve of RSF/TiO_2 fiber.

Table S1. Mechanical properties of De-silk and RSF/TiO_2 hybrid fibers

TiO_2 content (‰)	Stress/MPa	Modulus/GPa	Strain(%)	Breaking energy/MJ m^{-3}
0	168.5±15.0	2.9±0.4	36.5±7.7	52.1±16.4
0.5	170.7±14.2	3.8±0.6	44.0±6.8	55.7±10.1
1	171.3±16.1	4.1±0.2	88.3±10.3	93.1±27.1
3	201.8±11.3	4.2±0.8	63.8±10.4	89.8±17.5
5	218.5±12.1	5.9±0.7	37.7±4.8	54.1±12.6
7	161.7±27.1	7.0±1.5	31.8±4.1	38.7±11.8
Degummed silk [a)]	353.9±71.6	4.5±3.2	16.4±5.1	46.3±17.2

[a)] Data from our previous work[s1]

Supporting Equations and Derivations [s2-s7]

Guinier law is given by

$$I(q) = I_e n^2 \exp(-\frac{q^2 R_g^2}{3}) \quad \text{(S1)}$$

where $I(q)$ is the scattering intensity, I_e the X-ray scattering intensity of single electron, n the sum of electron in single particle, q the scattering vector ($q = 4\pi\sin\theta/\lambda$). Take the logarithm of Equation (S1):

$$\ln I(q) = K - \frac{R_g^2}{3} q^2 \quad \text{(S2)}$$

where constant K equals to $\ln I_e n^2$. Plot $\ln I(q)$ against to q^2, and the R_g can be obtained by

$$R_g = \sqrt{-3k} \quad \text{(S3)}$$

where k is the slope of $\ln I(q)$-q^2 curve. R_g is 15.9 nm calculated in this paper.

The fractal dimension is calculated as follows. According to the relationship between intensity $I(q)$ and fractal dimension:

$$I(q) = Kq^D \quad \text{(S4)}$$

where D is fractal dimension. Plot $\ln[I(q)]$ against $\ln q$, then the fractal dimension D can be obtained from the slope. The surface fractal dimension (D_s) can be calculated by

$$D_s = 6\text{-}D \quad \text{(S5)}$$

Modified Porod law is given by

$$I(q) = 2\pi I_e S(\rho_A - \rho_B)^2 q^{-4} \exp(-\sigma^2 q^2) \approx \frac{K_P}{q^4}(1 - \sigma^2 q^2) \quad \text{(S6)}$$

where S is the surface area of irradiated particles, ρ_A the electron density of A phase, ρ_B the electron density of B phase, σ the parameter of interphase thickness, K_P the coefficient after approximation. Plot $q^4 I(q)$ against to q^2, and σ can be obtained by

$$\sigma = \sqrt{k/b} \quad \text{(S7)}$$

where k is the slope of the negatively divergent part, b the extrapolated intercept. Similarly, Plot $q^2 I(q)$ against to q^{-2}, and σ can be obtained by

$$\sigma = \sqrt{b/k} \quad \text{(S8).}$$

The thickness of interface ΔR was approximately calculated by

$$\Delta R = 2\sqrt{3}\sigma \quad \text{(S9)}$$

where ΔR is calculated to 5.2 nm in this paper.

The particle is ellipsoidal with semiaxis of a 12 nm, b 12 nm, and c 25 nm obtained by TEM. ΔR is added to the dimensions of particle so that the semiaxes turn to a 17.5 nm, b 17.5 nm, and c 30.5 nm. According to the relationship between particle dimension and R_g

$$R_g = \left(\frac{a^2+b^2+c^2}{5}\right)^{1/2} = \left(\frac{17.5^2+17.5^2+30.5^2}{5}\right)^{1/2} = 15.6 \quad \text{(S10)}$$

Supporting Method

SR-WAXD data processing

FIT2D (V12.077) were applied to process SR-WAXD patterns. The circle center and distance of sample-to-detector are calibrated by CeO_2 powder. The background is subtracted. The radial bins are separated into 20~30 intervals. Each interval is azimuthally integrated. Plot the minimum intensity of azimuthally integrated profile against to 2θ so that the amorphous profile is obtained. Equatorial and meridianal integrations are done respectively. The patterns are indexed for a orthorhombic $P2_1$ space group with the unit cell of *a* 0.938 nm, *b* 0.949 nm and *c* 0.698 nm.[s8] Gaussians for equatorial peaks (010, 020, 210, 030) and meridianal peak (002) and determined amorphous profile are used to do deconvolution to obtain the crystallinity and crystallite size information. The calculation method of crystallinity and crystallite size can be found in reference.[s9] The content of interface/mesophase is calculated by the method suggested in reference.[s10] The azimuthal integration of (020/210) is done to get the orientation information of crystallite and interface/mesophase. The calculation method can be found in reference.[s10, s11]

SR-SAXS data processing

FIT2D (V12.077) and xPolar (V1.2.2.6) software were applied to process SR-SAXS patterns. The circle center and distance of sample-to-detector are calibrated by cowhells. The background is subtracted according to the value of ionization chambers. Integration is done to obtain the 1D SAXS pattern. Primus software is employed to calculate the R_g, and Gnom is used for $P(R)$ (particle size distribution function) calculation. Three-dimensional structure of scattering unit is constructed by DAMMIM software based on aforementioned procedures and the model is processed by PyMOL software.[s4, s5]

Supporting References

S1 M. J. Sun, Y. P. Zhang, Y. M. Zhao, H. L. Shao, X. C. Hu, *J. Mater. Chem.*, 2012, **22**, 18372.

S2 M. Roessle, D. Svergun, in *Encyclopedia of Biophysics*, (Ed: G. K. Roberts), Springer Berlin Heidelberg, 2013, 2382.

S3 O. Glatter, *Small Angle X-ray Scattering*. ACADEMIC PRESS INC., New York 1982.

S4 M. Rossle, P. Panine, V. S. Urban, C. Riekel, *Biopolymers*, 2004, **74**, 316.

S5 A. Martel, M. Burghammer, R. J. Davies, E. Di Cola, C. Vendrely, C. Riekel, *J. Am. Chem. Soc.*, 2008, **130**, 17070.

S6 L. D. Miller, S. Putthanarat, R. K. Eby, W. W. Adams, *Int. J. Biol. Macromol.*, 1999, **24**, 159.

S7 M. Canetti, A. Seves, F. Secundo, G. Vecchio, *Biopolymers*, 1989, **28**, 1613.

S8 Y. Takahashi, M. Gehoh, K. Yuzuriha, *Int. J. Biol. Macromol.*, 1999, **24,** 127.

S9 A. Martel, M. Burghammer, R. J. Davies, C. Riekel, *Biomacromolecules*, 2007, **8**, 3548.

S10 S. Sampath, T. Isdebski, J. E. Jenkins, J. V. Ayon, R. W. Henning, J. P. R. O. Orgel, O. Antipoa, J. L. Yarger, *Soft Matter*, 2012, **8**, 6713.

S11 D. T. Grubb, L. W. Jelinski, *Macromolecules*, 1997, **30**, 2860.